Site occupancy calibration of taxane pharmacology in live cells and tissues

Javier J. Pineda[a,1], Miles A. Miller[b], Yuyu Song[a], Hallie Kuhn[a], Hannes Mikula[b], Naren Tallapragada[a], Ralph Weissleder[b], and Timothy J. Mitchison[a,1]

[a]Department of Systems Biology, Harvard Medical School, Boston, MA 02115; and [b]Center for Systems Biology, Massachusetts General Hospital, Boston, MA 02114

Drug receptor site occupancy is a central pharmacology parameter that quantitatively relates the biochemistry of drug binding to the biology of drug action. Taxanes and epothilones bind to overlapping sites in microtubules (MTs) and stabilize them. They are used to treat cancer and are under investigation for neurodegeneration. In cells, they cause concentration-dependent inhibition of MT dynamics and perturbation of mitosis, but the degree of site occupancy required to trigger different effects has not been measured. We report a live cell assay for taxane-site occupancy, and relationships between site occupancy and biological effects across four drugs and two cell lines. By normalizing to site occupancy, we were able to quantitatively compare drug activities and cell sensitivities independent of differences in drug affinity and uptake/efflux kinetics. Across all drugs and cells tested, we found that inhibition of MT dynamics, postmitotic micronucleation, and mitotic arrest required successively higher site occupancy. We also found interesting differences between cells and drugs, for example, insensitivity of the spindle assembly checkpoint to site occupancy. By extending our assay to a mouse xenograft tumor model, we estimated the initial site occupancy required for paclitaxel to completely prevent tumor growth as 80%. The most important cellular action of taxanes for cancer treatment may be formation of micronuclei, which occurs over a broad range of site occupancies.

microtubules | taxane | epothilone | drug efficacy | micronuclei

Aunifying concept in the pharmacology of protein-binding drugs is site occupancy, the fraction of specific binding sites in a population of protein receptors that is bound by drug. The concentration of unbound drug at a site occupancy of 0.5 is called the K_d, which is used to compare the affinity of different drugs to the same site. Site occupancy is especially important when comparing drugs with different effects on the receptor (e.g., full vs. partial agonists). An efficacy parameter can be defined, which quantifies the effect of a drug on receptor function at a given site occupancy, usually 0.5 (1). The most common methods for measuring site occupancy are ligand displacement assays in which unlabeled test ligands compete with an easily measured labeled ligand for binding to the receptor. The labeled ligand is commonly radioactivity or fluorescence. If the K_d of the test ligand is known, the K_d of competing ligands can be inferred using the Cheng–Prusoff equation (2). Ligand displacement assays were invented for pure proteins and cell surface receptors, but they can be extended to the interior of living cells, notably using fluorescence technology (3). This allows direct measurement of biological actions as a function of site occupancy.

Here, we report a convenient fluorescent assay for measuring site occupancy of drugs that bind to the taxane and epothilone sites on microtubules (MTs) in living cells and use it to quantify biological effects as a function of site occupancy. The taxane site was defined using paclitaxel (Ptx), a natural product from the Pacific yew tree (4). Ptx and its derivative, docetaxel, are among the most active of solid tumor drugs and play a central role in combination chemotherapy (5). Development of new taxanes continues, with interest in derivatives with improved pharma-

cology and bioavailability (6), including improved brain penetration (7). There is also great interest in clinical development of alternative scaffolds that bind to the taxane site (8). Epothilones bind to an overlapping site in MTs and are naturally resistant to drug efflux pumps. One epothilone, ixabepilone (Ixa), is approved for cancer treatment (9).

Cancer is the only disease known to respond to taxanes or epothilones, but there has been significant interest in MT stabilization as a therapeutic modality in neurodegenerative disease (10). Epothilone D (EpoD) is particularly brain-penetrant and demonstrated promise in rodent models of neurodegeneration (11, 12). Cancer and neurodegeneration are very different diseases, and it seems likely that optimal therapeutic index might require different effects of drugs on the MT lattice. Given the interest in neuronal effects of taxane-site drugs, we tested if our approach could extend to a human neuron model.

The binding site for taxanes and epothilones on the interior of the MT has been well characterized at the atomic level (13, 14). Drug binding stabilizes the lattice, inhibits polymerization dynamics, and promotes ectopic MT nucleation. In dividing cells, these effects cause chromosome missegregation at lower drug concentrations and mitotic arrest at higher drug concentrations (4, 15, 16). In nondividing cells, they perturb organelle positioning, nuclear transport, and stress signaling (17–20). How these diverse cellular effects trigger tumor regression is controversial, with some authors favoring antimitotic mechanisms (21) and others interphase cell killing (20). No prior studies systematically measured multiple phenotypic effects in parallel as a

---

Significance

Taxanes are important for treating cancer and as tools in mitosis research, but mechanistic understanding has been limited by their complex pharmacology. They cause multiple biological actions, and it has been unclear how much drug bound to microtubules is needed for each action. We developed microscopy-based assays for measuring the fraction of specific binding sites occupied by taxanes in living cells as a function of drug concentration, and, in parallel, the different biological activities they cause. These assays will be useful for new drug development and suggest that the most important anticancer action of taxanes is postmitotic micronucleation.

function of drug concentration or quantified the degree of site occupancy required to cause each effect.

Medicinal chemistry of taxanes and epothilones has mostly been guided by IC_{50} metrics for cell proliferation and not by biochemical K_ds or efficacy parameters (22, 23). Another important metric has been sensitivity to drug efflux pumps (24). The most reliable biochemical K_d values come from the work of Andreu and Barasoain (25) and Díaz et al. (26), who measured displacement of a fluorescent taxane analog from cross-linked MTs using fluorescence polarization. These data quantified binding separately from effects on MT stability, and the resulting data were used to profile biochemical efficacy across panels of taxanes and epothilones (27, 28). This work significantly advanced taxane-site pharmacology but was difficult to relate to biological effects in living cells. Here, we report a live cell ligand displacement assay using the docetaxel derivative silicon rhodamine (SiR)-tubulin (SirTub), a low-affinity, fluorogenic, taxane-site ligand (29). Using this assay, we measured the degree of site occupancy required for perturbation of MT dynamics, chromosome missegregation, and mitotic arrest for representative taxane-site drugs. Our work agrees with a classic measurement of saturable binding of ^{3}H-Ptx in living cells, although that study used only one drug and did not measure biological effect (30). Furthermore, our fluorescence methodology is better suited to modern drug discovery pipelines since it does not require radioactivity.

Results

SirTub Can Be Displaced by Competing Drugs in Live Cells.
We preincubated RPE1 cells (Fig. 1A) and differentiated ReNcell VM human neurons (Fig. 1B) with 100 nM SirTub, and then added 100 nM EpoB and performed live fluorescence imaging. In both cell lines, specific signal decayed completely within 10 min of adding competitor, indicating rapid and complete ligand displacement; Fig. 1C quantifies this observation for RPE1 cells. To minimize possible complications from drug efflux pumps, all experiments were performed in the presence of 10 μM verapamil, an efflux pump inhibitor (31).

Binding constants are usually measured after equilibrium has been achieved for both probe and test ligands. To determine equilibration time, we measured the kinetics of SirTub uptake and binding in RPE1 (Fig. 1D) and HT1080 (*SI Appendix*, Fig. S1) cells. Automated thresholding and analysis allowed for ease of quantification (*SI Appendix*, Fig. S2). Signal from nonspecifically bound probe was significant (~40% at our standard probe concentration). In Fig. 1D and all subsequent experiments, 10 or more wells on each plate were reserved to measure nonspecific probe binding. Average fluorescence signal in the
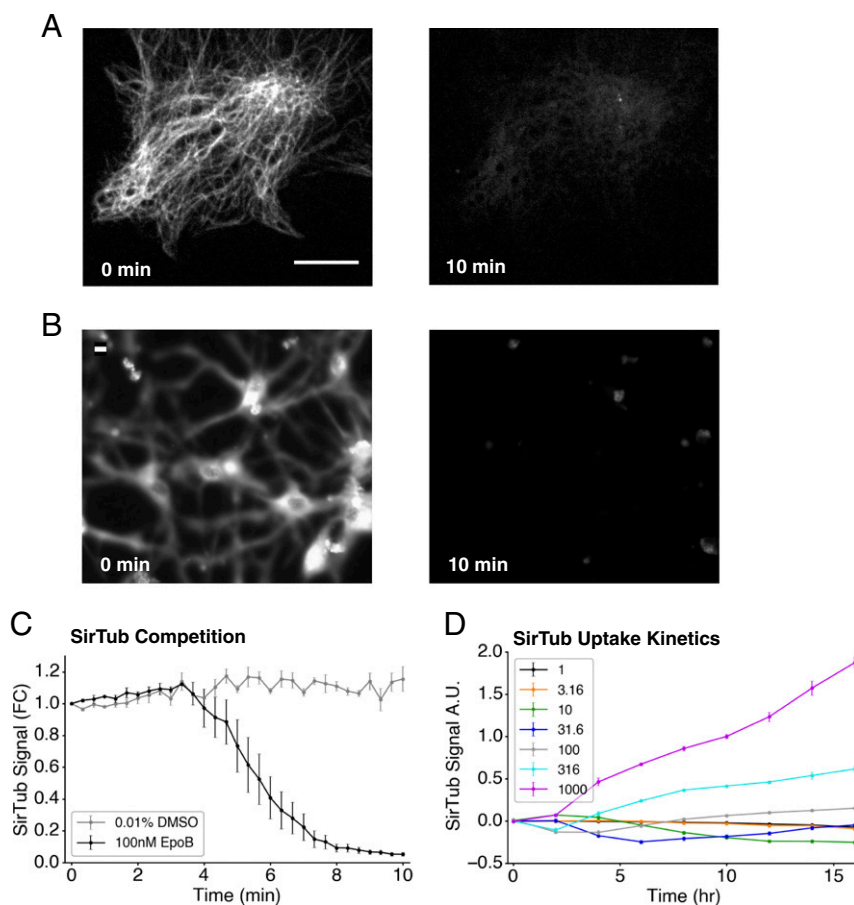
Fig. 1. SirTub can be displaced in live cells. (A) Representative images of RPE1 cells stained with SirTub before and after treatment with a competing drug (EpoB). Cells were incubated with 100 nM SirTub for 2.5 h, after which equimolar EpoB was added. (Scale bar: 10 μm.) (B) Representative images of ReNcell cells stained with SirTub before and after treatment with EpoB. Cells were incubated with 100 nM SirTub for 10 h, after which equimolar EpoB was added. (Scale bar: 10 μm.) (C) Quantification of SirTub displacement in A. SirTub signal was normalized by total cell area at every time point. FC, fold change. (D) Time course and titration of SirTub staining in RPE1 cells. The legend lists nanomolar concentrations of SirTub. Several wells were simultaneously treated with SirTub and equimolar EpoB to measure and subtract nonspecific probe binding. Intensities were normalized by cell area as in C, and then normalized with respect to 1 μM SirTub signal at 10 h. Each data point was averaged from at least nine wells. All error bars denote SEM. A.U., arbitrary unit.

presence of equimolar EpoB competitor (whose affinity is ~1,000-fold greater than that of probe) was subtracted from all values on the plate. Cellular uptake of SirTub was slow, and we were unable to saturate specific sites within 16 h over the dosage range tested, which was capped at 1 μM to avoid DMSO artifacts. This suggested a relatively large K_d for the probe. Unlabeled drugs reached equilibrium binding much faster at all concentrations (*SI Appendix*, Fig. S3 *A* and *B*). We chose a SirTub concentration (800 nM) and preincubation time (10–11 h) for site occupancy experiments where the signal was strong and changed negligibly during measurement. Lack of true equilibrium in probe binding precluded experimental measurement of probe K_d, but the resulting uncertainty in true probe K_d was not a problem. The much weaker affinity of the probe than test drugs meant that incomplete saturation with probe, or errors in probe K_d, had little effect on estimated test drug K_d. We verified this computationally by substituting a range of probe K_d values that were consistent with our data into the calculation of test drug K_d values and found little effect, provided the K_d value was much lower for the test drug than the probe.

SirTub Enables Site Occupancy Calibration in Multiple Cell Types. To calculate apparent K_ds of four drugs (Fig. 2*A*) from SirTub displacement curves, we first evaluated a classic Cheng–Prusoff competitive displacement model with a constant number of binding sites (Fig. 2*B*) and found less than ideal fits to the data. We traced the discrepancy to induction of MT polymerization by

test drugs, which caused an increase in binding sites when the test drug was titrated. This effect is evident from the slight upward trend before the decrease in Fig. 2*C*. It is characteristic of MT-stabilizing drugs and was accounted for in previous models of Ptx binding in living cells (29, 30). We therefore added a simple empirical model of drug-induced MT polymerization similar to the previous study (29). Our final model made use of two critical equations:

$$K_{d,app}^{d} = \frac{[D_{out}]}{\frac{[MT]_{tot}[P_{out}]}{[PMT]K_{d,app}^{p}} - \frac{[P_{out}]}{K_{d,app}^{p}} - 1}$$ [1]

$$S_d = \frac{[D_{out}]}{K_{d,app}^{d} + [D_{out}]}$$ [2]

In Eqs. **1** and **2**, S_d denotes site occupancy of competing drug, $[D_{out}]$ denotes external drug concentration, $K_{d,app}^{d}$ denotes apparent binding constant of competing drug, $[MT]_{tot}$ denotes total MT polymer, $[P_{out}]$ denotes external SirTub probe concentration, $[PMT]$ denotes concentration of probe-bound MT taxane sites (measured by fluorescence), and $K_{d,app}^{p}$ denotes the apparent binding constant of the SirTub probe. This model provided excellent fits (e.g., R^2 above 0.99 for all drugs in RPE1) to the ligand displacement data across four drugs and two cell lines (Fig. 2 *C* and *D*). Our binding model does not account for
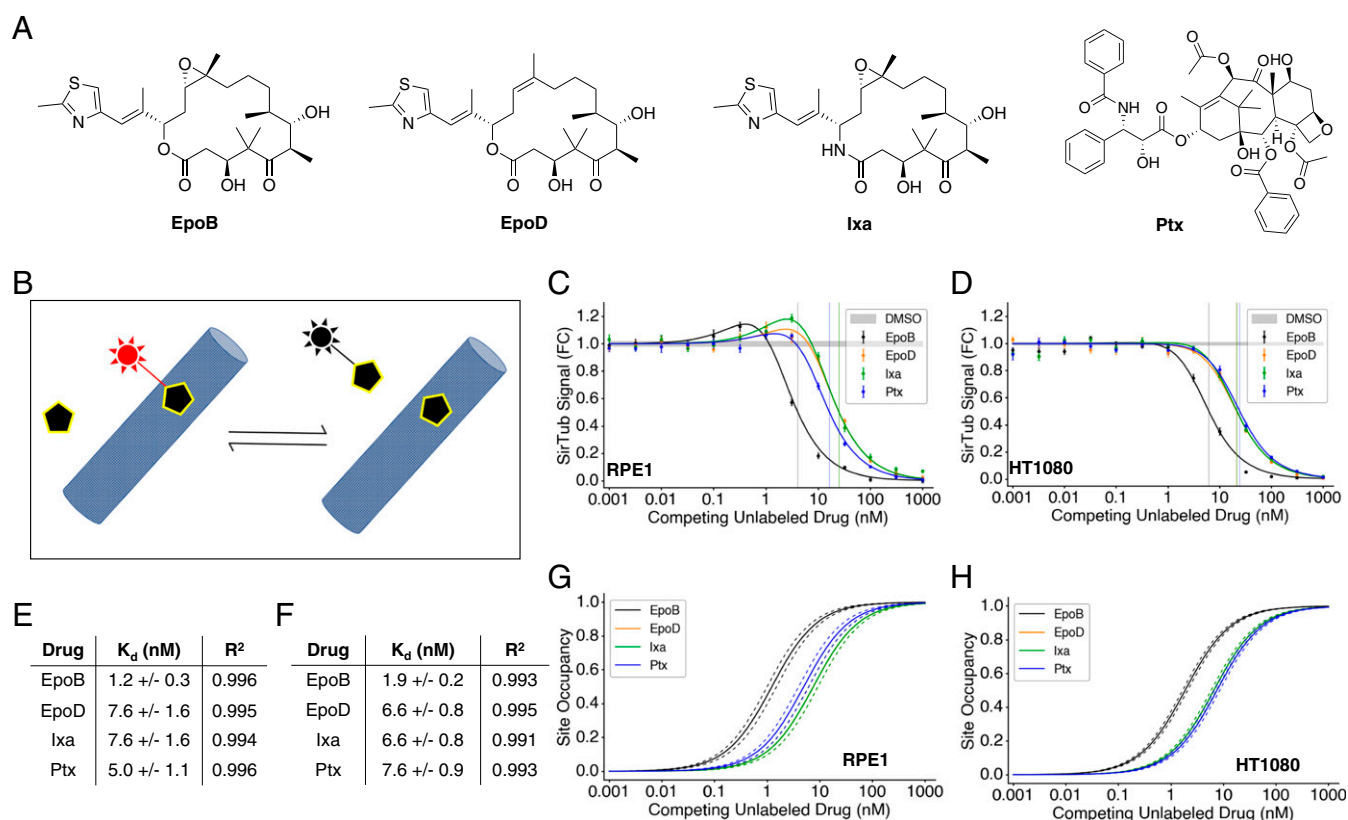

Fig. 2. SirTub can be used to determine binding constants of taxane-site drugs in live cells. (*A*) Chemical structures of EpoB, EpoD, Ixa, and Ptx. (*B*) Schematic of probe displacement assay. Probe fluorescence (red) is enhanced upon target binding. (*C*) SirTub displacement assay in RPE1 cells. Each data point was averaged from at least nine wells. Data were regressed using Eq. **1**, which accounts for drug-induced MT polymerization. IC$_{50}$s are denoted by solid vertical lines. FC, fold change. (*D*) SirTub displacement assay in HT1080 cells. Each data point was averaged from at least nine wells. Data were regressed as in *C*. (*E*) $K_{d,app}^{d}$ values for four drugs in RPE1 cells. Values were derived from the regressions present in *C*. (*F*) $K_{d,app}^{d}$ values for four drugs in HT1080 cells. Values were derived from the regressions present in *D*. (*G*) Site occupancy calibration curves for RPE1 cells. The $K_{d,app}^{d}$ values in *E* were input into Eq. **2** to compute drug-site occupancies. Dotted lines represent SE as derived from the model fit in *C*. (*H*) Site occupancy calibration curves for HT1080 cells. As in *G*, site occupancy values were derived from the $K_{d,app}^{d}$ values in *F*. Note that the Ixa curve is overlaid on the EpoD curve in *G* and *H*. All error bars denote SEM.

E

Drug	K_d (nM)	R^2
EpoB	1.2 +/- 0.3	0.996
EpoD	7.6 +/- 1.6	0.995
Ixa	7.6 +/- 1.6	0.994
Ptx	5.0 +/- 1.1	0.996

F

Drug	K_d (nM)	R^2
EpoB	1.9 +/- 0.2	0.993
EpoD	6.6 +/- 0.8	0.995
Ixa	6.6 +/- 0.8	0.991
Ptx	7.6 +/- 0.9	0.993

possible differences in the concentration of unbound drug outside and inside the cell. Therefore, all our K_d estimates are apparent K_ds, not true biochemical K_ds. We believe our values are close to the biochemical K_ds because we used a drug efflux pump inhibitor to minimize concentration differences across the plasma membrane, and our values are very similar to measured biochemical K_ds for some drugs (discussed below).

We used our model to regress the data (Fig. 2 C and D) and calculate apparent binding constants for four representative taxane-site ligands: EpoB, EpoD, Ixa, and Ptx (Fig. 2 E and F). Fig. 2 G and H shows curves for inferred binding-site occupancy as a function of external drug concentration in two cell lines, RPE1 (untransformed, telomerase reverse transcriptase-immortalized) and HT1080 (fibrosarcoma). EpoD and Ixa had almost the same apparent K_d values between the two cell lines according to our calculations (Fig. 2 E and F). Additionally, the apparent K_ds for EpoB and EpoD were very similar to measured biochemical K_ds for binding to glutaraldehyde cross-linked MTs in pure protein assays (27, 28, 32). Although our K_d estimates for Ptx differed substantially from the value obtained in some of these studies, they were in excellent agreement with the K_d of Ptx in living cells (5 nM) calculated from ^{3}H-Ptx binding in live MCF7 cells (30). Given recent interest in repurposing MT drugs for neuroprotective therapy (8, 33), we verified that we could obtain binding constants in differentiated ReNcell VM human neurons (*SI Appendix*, Fig. S4).

Site Occupancy Calibration of Three Cellular Phenotypes. We next quantified three MT- and cancer-relevant phenotypes that we could score by high-content imaging in living cells: MT polymerization dynamics, mitotic arrest, and mitosis-dependent micronucleation. MT dynamics were quantified by imaging stably transfected EB3-GFP (RPE1 only), which tacks growing plus ends (Fig. 3A and *SI Appendix*, Fig. S5). This provides a sensitive and specific assay of plus end dynamics (34). Stabilizing drugs deplete soluble tubulin, and thus block plus end growth and formation of EB3 comets. Mitotic arrest was measured by rounded morphology of living cells using EB3-GFP signal for RPE1 (Fig. 3B) or by adding a cell-permeant dye, SiR-eribulin, for HT1080 (*SI Appendix*, Fig. S6). Micronucleation, which might be particularly relevant for solid tumor responses, was measured by imaging a cell-permeant DNA dye (Fig. 3C and *SI Appendix*, Fig. S7). Nuclear morphology was complex after exit from abnormal mitosis, with many clustered micronuclei that were difficult to segment with simple thresholding methods (Fig. 3C, Inset). Watershed segmentation significantly improved the segmentation of micronuclei (*SI Appendix*, Fig. S7). It was not possible to segment every micronucleus present due to overlap in 2D images, but we segmented the majority as judged by eye. The number of segmentable DNA particles per unit area generated reliable dose–response curves. Fig. 3D shows phenotypes as a function of EpoD concentration, with the x axis scaled to be linear in site occupancy and the y axis scaled to the normalized
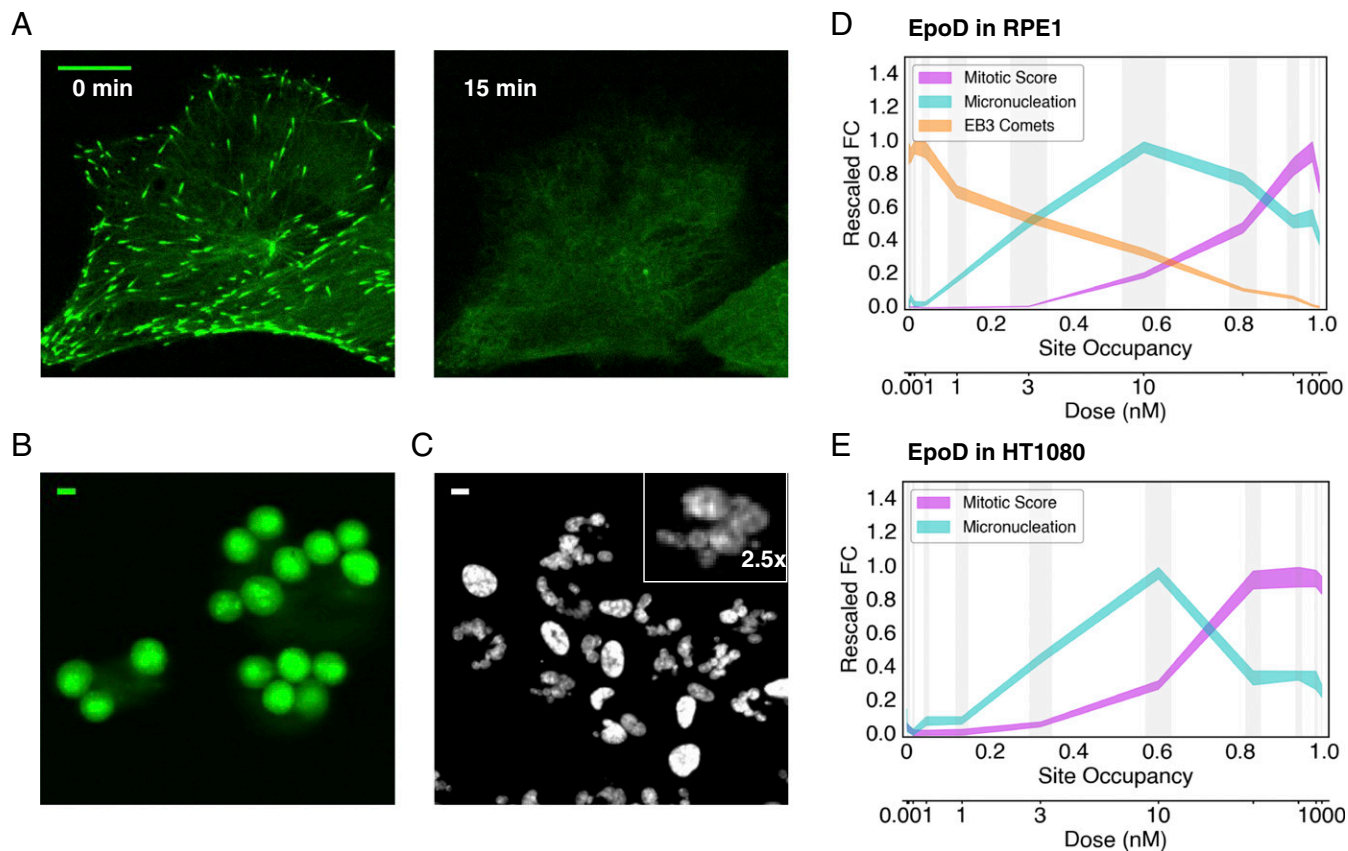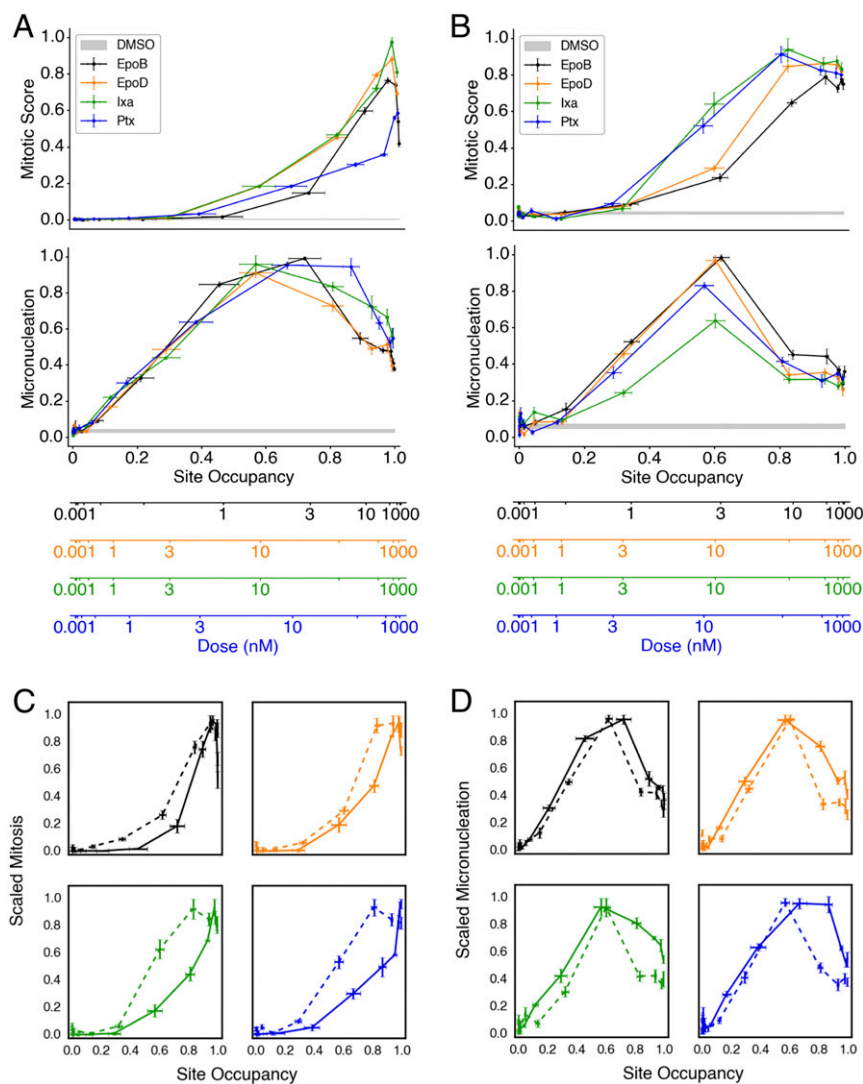

Fig. 3. Phenotypic comparisons on the site occupancy axis. (A) EB3 comets in RPE1 cells before and after treatment with 100 nM EpoB. (Scale bar: 10 μm.) (B) RPE1 cells arrested in mitosis 22 h after treatment with 30 nM EpoB. The EB3-GFP channel is shown. (Scale bar: 10 μm.) (C) Micronucleated RPE1 cells 22 h after treatment with 1 nM EpoB. (Scale bar: 10 μm.) The Hoechst channel is shown. (Magnification: Inset, 2.5×.) (D) Phenotypic comparison of EB3 comet loss, micronucleation, and mitotic arrest in RPE1 cells treated with EpoD. Phenotypic measurements are scaled to facilitate comparison and are shown with their corresponding SEs (indicated by line thickness). Drug dose calibration is shown. Vertical gray bars denote SE of site occupancy. FC, fold change. (E) Phenotypic comparison of micronucleation and mitotic arrest in HT1080 cells treated with EpoD. Phenotypic measurements have been scaled as in D. Each value shown in D and E was averaged from nine replicate wells.

fold change of phenotype metrics. Fig. 3E shows mitosis and micronucleus phenotypes in HT1080 cells (here, we lacked a bright EB3-GFP line). We performed quantitative phenotypic comparisons for all four drugs in both RPE1 (*SI Appendix*, Fig. S8) and HT1080 (*SI Appendix*, Fig. S9) cells.

Plus end dynamics were the most sensitive phenotype, with loss of EB3 comets first detected at a site occupancy of ∼0.1 and a steady decrease to zero comets at a site occupancy of ∼1.0. Micronucleation was the second most sensitive phenotype, first increasing at a site occupancy of ∼0.1–0.2 and peaking at a site occupancy of ∼0.6. Micronucleation declined at higher site occupancies, presumably because mitotic arrest slowed progression into micronucleated G1. We scored micronucleation at 22 h for RPE1 and 24 h for HT1080, the approximate doubling times for each line. This reduced complications from apoptosis. Cells arrested in mitosis eventually slip out of mitosis and progress to micronucleation or/and apoptosis over 2–3 d. Mitotic arrest required higher site occupancies and was maximal at a site occu-

pancy above 0.8 in both cell lines. Mitotic arrest decreased at very high external drug concentrations, where site occupancy increased above 0.95, but we suspect our model, which assumes uniform affinity of binding sites, is no longer accurate in this regime. A notable feature of our data is the presence of a regime that exhibits strong perturbation of MT dynamics and micronucleation, but weak induction of mitotic arrest, at site occupancies of ∼0.1–0.6 in both cell lines. This low-dose regime, where mitotic perturbation occurs without mitotic arrest, has been noted previously and may be of therapeutic importance (15, 16).

Taxane-Site Drugs Differ Across Phenotypes and Cell Lines. Fig. 4 presents all our data for micronucleation and mitotic arrest in plots chosen to facilitate comparison between drugs (Fig. 4 *A* and *B*) or between cells (Fig. 4 *C* and *D*). In each case, the phenotypic data are plotted as a function of site occupancy so that we can directly compare drugs or cells. Broadly speaking, the four drugs were similar in their ability to promote micronucleation at lower site occupancies and mitotic arrest at higher


Fig. 4. Drug- and cell-type comparisons on the site occupancy axis. (*A*) Drug–drug comparisons by mitotic arrest and micronucleation in RPE1 cells. All *y*-axis values are scaled to the maximum and minimum observed in the cell line. Dose calibration axes are included for each drug tested. (*B*) Drug–drug comparisons by mitotic arrest and micronucleation in HT1080 cells. All *y*-axis values are scaled as in *A*. (*C*) Cell-type comparison between RPE1 (solid lines) and HT1080 (dotted lines) cells by mitotic arrest. Mitotic scores have been scaled to the maximum and minimum observed for each drug. (*D*) Cell-type comparison between RPE1 (solid lines) and HT1080 (dotted lines) cells by micronucleation. Micronucleation values have been scaled to the maximum and minimum observed for each drug. Each value shown in *A–D* was averaged from nine replicate wells. All error bars denote SEM.

site occupancies. That said, we also observed differences. Ptx is less efficient at promoting mitotic arrest than the epothilones in RPE1 but is one of the most efficient arresters in HT1080 cells at intermediate site occupancies (Fig. 4 *A* and *B*). We did not observe any significant differences in mitotic maxima in HT1080 cells (*SI Appendix*, Fig. S10). Also, although there is no difference in micronucleation among the drugs in RPE1, these values differed significantly in HT1080, with Ixa significantly less efficient than the other drugs (Fig. 4 *A* and *B* and *SI Appendix*, Fig. S11).

Normalizing Drugs to Site Occupancy Reveals Differential Cellular Sensitivity. Comparing between cell lines, and plotting the *y* axis normalized to maximal fold change to facilitate comparison, we noted one major difference across all four drugs. HT1080 cells exhibited mitotic arrest at lower site occupancy than RPE1 cells (Fig. 4*C*). The onset of micronucleation was similar in the two cell lines, but the postpeak decrease shifted to lower values

in HT1080 because increased mitotic arrest, which decreased micronucleation at 24 h, initiates at lower site occupancy (Fig. 4*D*). We especially observed this leftward shift in HT1080 with Ixa and Ptx. This result suggests that the spindle assembly checkpoint is more sensitive to MT stabilization in HT1080 cells.

High Initial Site Occupancy Is Needed to Prevent Tumor Growth. A critical question from a clinical perspective is the minimal site occupancy required in vivo for therapeutic efficacy. In mice, the dose of Ptx required to promote tumor regression is 10–40 mg/kg, depending on the tumor, schedule, and vehicle (35–37). We adapted our fluorescence assay to a highly responsive HT1080 xenograft tumor model that we used previously to probe cellular actions of Ptx (38, 39). Nu/nu mice with HT1080 tumors were dosed i.v. with Ptx or cremophor vehicle, followed 1 h later by SirTub. Tumors were excised 24 h after Ptx treatment and immediately imaged ex vivo by confocal microscopy. Fig. 5*A*
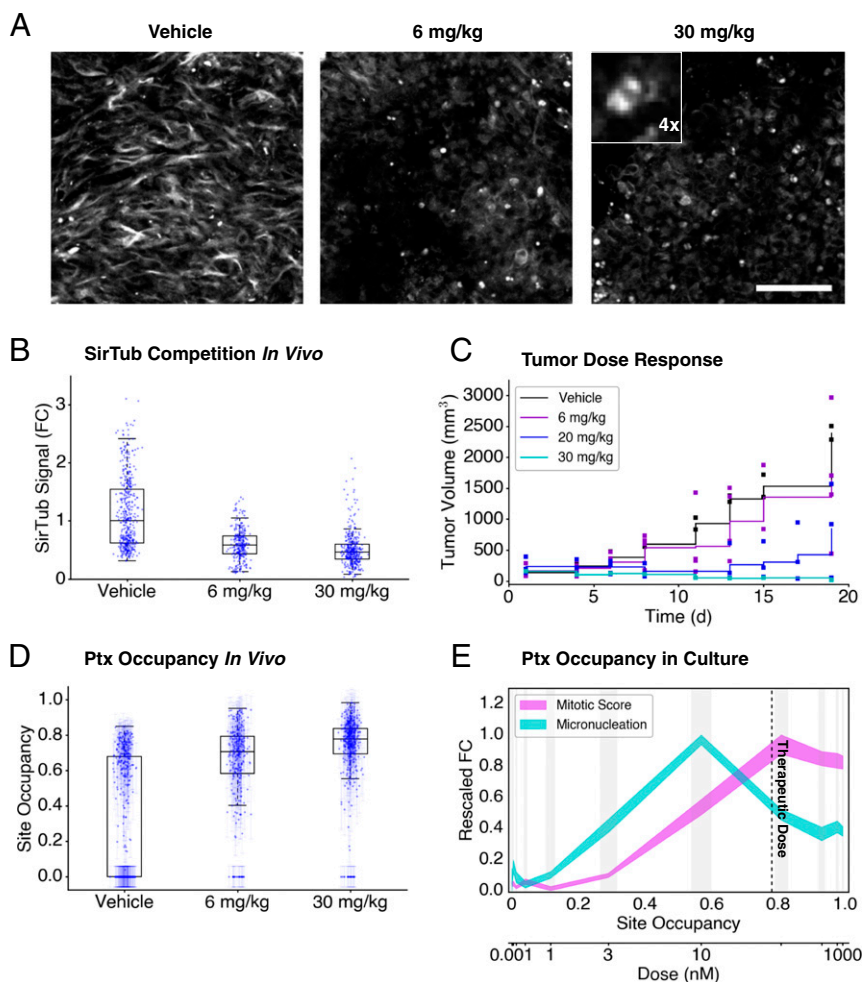
Fig. 5. Taxane-site occupancy in vivo. (*A*) Ex vivo images of SirTub in an HT1080 xenograft tumor 24 h after infusion of vehicle control (*Left*), 6 mg/kg of Ptx (*Center*), and 30 mg/kg of Ptx (*Right*). (Scale bar: 100 μm.) (*Inset*) Mitotic cell labeled with SirTub. (Magnification: 4×.) (*B*) SirTub displacement in HT1080 xenograft tumors 24 h after Ptx treatment. Each data point denotes a single cell. FC, fold change (i.e., all values are normalized by the average SirTub signal in the vehicle control). (*C*) Response of HT1080 xenograft tumors to single treatments with Ptx. Once palpable tumors were established, mice were treated on day 0 with a single i.v. dose of Ptx in cremophor EL as indicated. Each square denotes a single measurement of a mouse tumor (two, four, three, and one tumors were used for vehicle, 6 mg/kg, 20 mg/kg, and 30 mg/kg, respectively). Solid lines track average tumor volume. (*D*) All data points in *B* have been converted to site occupancy measurements using the data in Fig. 2 *C* and *G*. At the indicated doses, drug-induced MT polymerization was assumed to be one- to twofold compared with basal polymer. SE bars are shown in lighter blue at each data point. (*E*) Phenotypic comparison of micronucleation and mitotic arrest in HT1080 cells treated with Ptx. The dotted line represents the predicted intratumoral site occupancy. Phenotypic measurements are scaled to facilitate comparison, and are shown with their corresponding SEs (indicated by line thickness). Drug dose calibration is shown. Vertical gray bars denote SE of site occupancy. Each value shown in *E* was averaged from nine replicate wells.

shows SirTub images. Mitotic spindles were clearly visualized (Fig. 5A, inlet). We were unable to resolve single MTs in interphase cells, but they exhibited specific (i.e., Ptx-compatible) cytoplasmic signal that we could quantify by microscopy. Fig. 5B shows quantification of probe displacement in single cells from multiple fields and tumors in three mice at two doses of competing drug. Competition was dose-dependent: 30 mg/kg of Ptx reduced SirTub signal by ~50%, on average, with considerable heterogeneity among single cells. To confirm that our HT1080 xenografts respond in the typical range, we performed a small single-dose study and found that 6 mg/kg and 20 mg/kg of i.v. Ptx reduced HT1080 tumor growth to a variable extent and 30 mg/kg blocked growth completely (Fig. 5C). We applied the site occupancy calibration data that we previously obtained for HT1080 cells (Fig. 2H) to convert every SirTub measurement from Fig. 5B into a site occupancy estimate (Fig. 5D). Since we did not know the concentration of SirTub in the tumor, we considered a range for possible extracellular in vivo SirTub concentrations (i.e., 10–800 nM) and accounted for a one- to twofold increase in MT polymer in vivo after addition of Ptx (*SI Appendix*, Fig. S12). By this analysis, we estimate the in vivo site occupancy for the curative 30-mg/kg dose of Ptx as being ~0.8 at 24 h (Fig. 5D). We previously measured peak mitotic arrest values of ~5–10% of cells ~24 h after a 30-mg/kg Ptx dose in HT1080 xenografts and peak micronucleation values of ~25–30% of cells at ~72 h (39). We conclude that the minimal curative dose of Ptx in the HT1080 model corresponds to an initial site occupancy of ~0.8 in the tumor, which triggers mitotic arrest at peak drug concentration, followed by micronucleation as site occupancy declines through dissociation from binding sites and clearance from circulation (Fig. 5E).

Discussion

A ligand displacement assay in live cells allowed us to calculate taxane-site occupancy as a function of extracellular concentration for four drugs in two cell lines. Our inferred K_d values were similar to published K_ds measured using conceptually similar fluorescent ligand displacement assays on pure MTs (27) and live cell binding of ^{3}H-Ptx (30). Previous work mostly measured phenotypic effects of taxane-site drugs as a function of external drug concentration or specific phenotypes at saturating drug concentration (22, 40). Our work allows more precise comparisons of biological effects across external concentrations, drug analogs, and cell types.

A possible point of confusion in taxane-site pharmacology is the relationship between the concentration of free and total drug inside cells. Taxanes accumulate in cells and tumors, so their total concentration inside cells far exceeds the concentration in medium or plasma (30, 41). Total drug is the sum of free, specifically bound, and nonspecifically bound drug. We could not quantify nonspecific binding of nonfluorescent drugs, but we corrected all our data for nonspecific binding of probe. Specifically bound drug can be calculated from our data by multiplying our site occupancy values by binding-site concentration. Tubulin constitutes ~4% of total protein in HeLa cells (42), corresponding to ~20 μM, and most of it polymerizes when taxanes or epothilones are added. Given the apparent K_ds of the drugs we tested, the concentration of specifically bound, unlabeled drug is thus three to four orders of magnitude higher than unbound drug, consistent with previous data using ^{3}H-Ptx binding (30).

Our data revealed a clear rank order in sensitivity of phenotypic effects to site occupancy. Loss of MT dynamics was the most sensitive, with detectable perturbation starting at a site occupancy of ~0.1, followed by micronucleation starting at ~0.2 and mitotic arrest requiring 0.6–1.0. This rank order was similar for all four drugs in both cell lines. Substoichiometric binding of Ptx was previously shown to inhibit polymerization dynamics (43), consistent with our findings. Previous work also

showed that chromosome segregation defects and micronucleation occur at lower concentrations of Ptx than mitotic arrest (15, 16). The mechanism of micronucleation is unclear, and probably involves a combination of ectopic spindle pole formation (16) and ectopic cleavage furrow assembly (44). Mitotic arrest decreased at the highest external drug concentrations we tested and at the highest inferred site occupancies (>0.95). Caution is required in interpreting these high site occupancy values, since our model assumes homogeneous binding sites, and very high drug concentration might access additional, lower affinity sites (e.g., on exposed plus ends). Decreased duration of mitotic arrest at Ptx concentrations above 1 μM was noted previously and attributed to stabilization of syntelic kinetochore attachments (45). This bell-shaped dose–response is interesting but unlikely to be relevant to chemotherapy, since mitotic arrest only decreased at Ptx concentrations that exceed safe plasma concentrations (16, 41).

We asked if taxane-site drugs differ in their phenotypic actions once normalized by site occupancy, which compares efficacy independent of K_d. Comparing across drugs in RPE1 (Fig. 4A) and HT1080 (Fig. 4B) cells, we noted overall similar efficacies but some interesting differences (e.g., more efficient mitotic arrest by Ptx and Ixa in HT1080). While EpoD and Ixa had identical apparent K_d values in HT1080 cells, their phenotypic effects differed noticeably, suggesting different efficacies. However, these differences were not seen in RPE1 cells. Future analysis across more diverse structure-activity relationship (SAR) series might reveal larger efficacy differences.

A central question in taxane-site pharmacology is which phenotypic effects are responsible for tumor regression. This is a complex issue, with different authors favoring chromosome loss via aberrant mitosis (21), bystander killing (46), and direct cytotoxic actions on nondividing cells (20). Our work does not address this question directly, but it provides additional information. In particular, we confirm that micronucleation occurs at lower concentrations than mitotic arrest for all drugs, and therefore might predominate in tumors. Standard Ptx doses are sufficient to cause mitotic arrest in tumors 24 h after drug infusion (47), but plasma drug concentrations decrease rapidly due to drug clearance between doses. Micronuclei trigger postmitotic inflammatory signaling (48, 49). This may allow a subset of tumor cells that pass through mitosis in drug to cause regression of the whole tumor in sensitive patients via recruitment of cytotoxic leukocytes and/or inflammatory damage to the neovasculature (50).

To connect our work to in vivo pharmacology, we measured the Ptx dose required to cure a sensitive xenograft tumor model, and then estimated site occupancy in tumor cells 24 h after this dose (Fig. 5). We observed a 50% decrease in SirTub signal at the curative 30-mg/kg dose. Our calculations suggest that the in vivo site occupancy of SirTub was below 0.2 in the absence of drug; thus, in the presence of 30 mg/kg of Ptx, SirTub occupancy would decrease to below 0.1, leaving up to 90% of taxane sites for Ptx to bind. This is mathematically consistent with our data and suggests that a relatively high initial Ptx-site occupancy, ~0.8, was required for cure following a single dose in this model. How does this relate to human patients? A recent study assessed the intratumoral and plasma concentration of Ptx in patients with breast cancer as 1.1–9 μM and 80–280 nM, respectively, 20 h after infusion of Ptx (16). Intratumoral concentrations measure the sum of free, specifically, and nonspecifically bound drug, and their interpretation is difficult. If we assume the plasma concentration is close to the extracellular concentration, and drug efflux pumping is not a major issue, then we can estimate site occupancy using our data. Extracellular Ptx at a concentration of 80–280 nM should generate a site occupancy greater than 0.8 (Fig. 2 G and H). This is in the concentration regime that promotes mitotic arrest (Fig. 5E), consistent with elevated mitotic

index at 24 h post-Ptx in human tumors (47). However, micronucleation will likely predominate at later time points as initially arrested cells slip into micronucleated interphase, and cells that newly enter mitosis do so at drug concentrations that are lower due to clearance. Even at 30 mg/kg of Ptx in HT1080 xenograft tumors, micronucleation strongly predominated over mitotic arrest at 72 h postdrug (39).

Our work sheds light on taxane pharmacology and demonstrates the potential of site occupancy measurements to guide future medicinal chemistry, whether for treatment of cancer or neurological diseases. It informs, but does not answer, the long-standing question of how taxanes promote regression of solid tumors. Based on the predominance of micronucleation over a broad range of site occupancies, we currently favor an inflammatory micronucleation model of taxane action (50).

Materials and Methods

Cell Culture. RPE1 cells expressing EB3-GFP were maintained in DMEM/F12 (Life Technologies) and supplemented with 10% (vol/vol) FBS (GIBCO) and 1% penicillin-streptomycin (Cellgro). HT1080 cells expressing EB3-mApple were grown in DMEM (Cellgro) supplemented with 10% FBS and 1% penicillin-streptomycin. ReNcell VM human neural progenitor cells (Millipore) were grown in ReNcell NSC maintenance medium supplemented with EGF and bFGF and differentiated into dopaminergic neurons in growth factor-free medium for 14 d.

Image Acquisition. For the initial proof-of-principle SirTub competition experiment (Fig. 1A), we used a spinning-disk confocal microscope (Nikon) equipped with a 60×/1.42-N.A. plan apochromat objective, heated chamber, and MetaMorph acquisition software. For Fig. 1C, the final time point was used to determine the nonspecific signal of SirTub, after which the non-specific signal value was subtracted from all preceding time points. For all other SirTub experiments, we imaged cells using an InCELL Analyzer 6000 high-content microscope (GE Healthcare Life Sciences), equipped with 40×/0.95-N.A. (for EB3 comet imaging) and 20×/0.75-N.A. (for all other imaging) plan apochromat objectives, a heated stage, and a heated lid, as well as constant CO_2 flow. For SirTub, Hoechst, and EB3 imaging, optimal focal planes were determined using the auto-offset function in the InCELL software. For imaging of mitotic cells, the auto-offset parameter was raised by 10 μm to blur out nonmitotic cells and put mitotic cells in focus. Rounded geometry was then used to segment the mitotic cells. Confocality was used for all imaging except nuclear area quantification, and 2×2 binning was used for all imaging except EB3 imaging.

Live Cell Microscopy. For spinning-disk SirTub imaging, RPE1 cells were imaged on 35-mm plates at 20–30% confluency. For high-content imaging, RPE1 and HT1080 cells were seeded at 5,000 cells per well in 20 μL of serum-free medium on 384-well optical bottom Cell Carrier plates (PerkinElmer) coated with Cell-Tak (Corning). After 45 min, 20 μL of medium with 20% FBS was added to each well. After 4 h, 40 μL of medium containing 10% FBS, 20 μM verapamil, and 2× SirTub (for SirTub plates only) was added to each well. Competing drugs were dispensed immediately after verapamil addition using a D300 Digital Dispenser (Hewlett-Packard). SirTub was found to be aggregate-prone, which would result in inconsistent probe distribution by the D300 Digital Dispenser. For this reason, SirTub was thawed, vortexed vigorously, centrifuged at $20,000 \times g$ for 10 min, and carefully transferred to medium, which was then manually pipetted on the imaging plates before drug treatments. Final DMSO concentrations were kept below 0.02%. Image acquisition was started immediately after drug treatments except for the EB3 comet experiments; for these experiments, one time point was acquired before drug addition.

In Vivo SirTub Competition and Microscopy. All animal research was performed in accordance with the guidelines from the Institutional Sub-committee on Research Animal Care. Two million HT1080-H2B-mApple cells were implanted s.c. into female nu/nu mice at 4–6 wk of age. Roughly 2 wk later, the indicated dose of Ptx or vehicle was administered i.v. in DMAC/solutol and PBS from a DMSO stock solution; 1 h later, 300 nmol of SirTub was administered using the same i.v. formulation. Twenty-four hours following taxane treatment, tumors were excised and immediately imaged. Before harvesting, 10 kDa of dextran-Pacific Blue and 2 MDa of FITC-dextran were coadministered i.v. to confirm vascular perfusion to the tumor as an inclusion criterion. Data for each condition were obtained from at least 250 cells across at least three tumors. Tumor microscopy was performed on an Olympus FV1000 confocal-multiphoton imaging system, with a XLUMPLFLN 20× water immersion objective (N.A. = 1.0; Olympus America); 2× digital zoom; sequential scanning using 405-nm, 473-nm, 559-nm, and 635-nm diode lasers and a DM405/473/559/635-nm dichroic beam splitter; and collection of emitted light using beam splitters (SDM473, SDM560, and SDM 640; all from Olympus America) and emission filters BA430-455, BA490-540, BA575-620, and BA655-755; all from Olympus America).

Taxane-Site Relevant Python and ImageJ Coding for Image Quantification and Analysis. All relevant coding is freely available at https://github.com/JavierJPineda/TaxaneOccupancy.

1. Black JW, Leff P (1983) Operational models of pharmacological agonism. *Proc R Soc Lond B Biol Sci* 220:141–162.
2. Cheng Y, Prusoff WH (1973) Relationship between the inhibition constant (K1) and the concentration of inhibitor which causes 50 per cent inhibition (I50) of an enzymatic reaction. *Biochem Pharmacol* 22:3099–3108.
3. Stoddart LA, White CW, Nguyen K, Hill SJ, Pfleger KD (2016) Fluorescence- and bioluminescence-based approaches to study GPCR ligand binding. *Br J Pharmacol* 173:3028–3037.
4. Horwitz SB (1994) Taxol (paclitaxel): Mechanisms of action. *Ann Oncol* 5(Suppl 6):S3–S6.
5. Skeel RT, Khleif SN, eds (2011) *Handbook of Cancer Chemotherapy* (Lippincott Williams & Wilkins, Philadelphia).
6. Yared JA, Tkaczuk KHR (2012) Update on taxane development: New analogs and new formulations. *Drug Des Devel Ther* 6:371–384.
7. Fitzgerald DP, et al. (2012) TPI-287, a new taxane family member, reduces the brain metastatic colonization of breast cancer cells. *Mol Cancer Ther* 11:1959–1967.
8. Rohena CC, Mooberry SL (2014) Recent progress with microtubule stabilizers: New compounds, binding modes and cellular activities. *Nat Prod Rep* 31:335–355.
9. Hunt JT (2009) Discovery of ixabepilone. *Mol Cancer Ther* 8:275–281.
10. Brunden KR, et al. (2011) The characterization of microtubule-stabilizing drugs as possible therapeutic agents for Alzheimer's disease and related tauopathies. *Pharmacol Res* 63:341–351.
11. Barten DM, et al. (2012) Hyperdynamic microtubules, cognitive deficits, and pathology are improved in tau transgenic mice with low doses of the microtubule-stabilizing agent BMS-241027. *J Neurosci* 32:7137–7145.
12. Zhang B, et al. (2012) The microtubule-stabilizing agent, epothilone D, reduces axonal dysfunction, neurotoxicity, cognitive deficits, and Alzheimer-like pathology in an interventional study with aged tau transgenic mice. *J Neurosci* 32:3601–3611.
13. Prota AE, et al. (2013) Molecular mechanism of action of microtubule-stabilizing anticancer agents. *Science* 339:587–590.
14. Kellogg EH, et al. (2017) Insights into the distinct mechanisms of action of taxane and non-taxane microtubule stabilizers from cryo-EM structures. *J Mol Biol* 429:633–646.
15. Jordan MA, et al. (1996) Mitotic block induced in HeLa cells by low concentrations of paclitaxel (Taxol) results in abnormal mitotic exit and apoptotic cell death. *Cancer Res* 56:816–825.
16. Zasadil LM, et al. (2014) Cytotoxicity of paclitaxel in breast cancer is due to chromosome missegregation on multipolar spindles. *Sci Transl Med* 6:229ra43.
17. Soltys BJ, Gupta RS (1992) Interrelationships of endoplasmic reticulum, mitochondria, intermediate filaments, and microtubules–A quadruple fluorescence labeling study. *Biochem Cell Biol* 70:1174–1186.
18. Wang TH, et al. (1999) Microtubule dysfunction induced by paclitaxel initiates apoptosis through both c-Jun N-terminal kinase (JNK)-dependent and -independent pathways in ovarian cancer cells. *J Biol Chem* 274:8208–8216.
19. Darshan MS, et al. (2011) Taxane-induced blockade to nuclear accumulation of the androgen receptor predicts clinical responses in metastatic prostate cancer. *Cancer Res* 71:6019–6029.
20. Komlodi-Pasztor E, Sackett D, Wilkerson J, Fojo T (2011) Mitosis is not a key target of microtubule agents in patient tumors. *Nat Rev Clin Oncol* 8:244–250.
21. Weaver BA (2014) How Taxol/paclitaxel kills cancer cells. *Mol Biol Cell* 25:2677–2681.
22. Altmann KH, Pfeiffer B, Arseniyadis S, Pratt BA, Nicolaou KC (2007) The chemistry and biology of epothilones–The wheel keeps turning. *ChemMedChem* 2:396–423.

PHARMACOLOGY

23. Altmann KH, Gaugaz FZ, Schiess R (2011) Diversity through semisynthesis: The chemistry and biological activity of semisynthetic epothilone derivatives. *Mol Divers* 15:383–399.

24. Chou TC, et al. (1998) Desoxyepothilone B: An efficacious microtubule-targeted antitumor agent with a promising in vivo profile relative to epothilone B. *Proc Natl Acad Sci USA* 95:9642–9647.

25. Andreu JM, Barasoain I (2001) The interaction of baccatin III with the taxol binding site of microtubules determined by a homogeneous assay with fluorescent taxoid. *Biochemistry* 40:11975–11984.

26. Díaz JF, Strobe R, Engelborghs Y, Souto AA, Andreu JM (2000) Molecular recognition of taxol by microtubules. Kinetics and thermodynamics of binding of fluorescent taxol derivatives to an exposed site. *J Biol Chem* 275:26265–26276.

27. Buey RM, et al. (2004) Interaction of epothilone analogs with the paclitaxel binding site: Relationship between binding affinity, microtubule stabilization, and cytotoxicity. *Chem Biol* 11:225–236.

28. Buey RM, et al. (2005) Microtubule interactions with chemically diverse stabilizing agents: Thermodynamics of binding to the paclitaxel site predicts cytotoxicity. *Chem Biol* 12:1269–1279.

29. Lukinavičius G, et al. (2014) Fluorogenic probes for live-cell imaging of the cytoskeleton. *Nat Methods* 11:731–733.

30. Kuh H-J, Jang SH, Wientjes MG, Au JL (2000) Computational model of intracellular pharmacokinetics of paclitaxel. *J Pharmacol Exp Ther* 293:761–770.

31. Bellamy WT (1996) P-glycoproteins and multidrug resistance. *Annu Rev Pharmacol Toxicol* 36:161–183.

32. Dietrich SA, et al. (2009) Epothilone analogues with benzimidazole and quinoline side chains: Chemical synthesis, antiproliferative activity, and interactions with tubulin. *Chemistry* 15:10144–10157.

33. Brunden KR, Trojanowski JQ, Smith AB, 3rd, Lee VM, Ballatore C (2014) Microtubule-stabilizing agents as potential therapeutics for neurodegenerative disease. *Bioorg Med Chem* 22:5040–5049.

34. Stepanova T, et al. (2003) Visualization of microtubule growth in cultured neurons via the use of EB3-GFP (end-binding protein 3-green fluorescent protein). *J Neurosci* 23:2655–2664.

35. Rose WC (1993) Taxol-based combination chemotherapy and other in vivo preclinical antitumor studies. *J Natl Cancer Inst Monogr* 15:47–53.

36. Milross CG, et al. (1996) Relationship of mitotic arrest and apoptosis to antitumor effect of paclitaxel. *J Natl Cancer Inst* 88:1308–1314.

37. Desai N, et al. (2006) Increased antitumor activity, intratumor paclitaxel concentrations, and endothelial cell transport of cremophor-free, albumin-bound paclitaxel, ABI-007, compared with cremophor-based paclitaxel. *Clin Cancer Res* 12:1317–1324.

38. Orth JD, et al. (2011) Analysis of mitosis and antimitotic drug responses in tumors by in vivo microscopy and single-cell pharmacodynamics. *Cancer Res* 71:4608–4616.

39. Chittajallu DR, et al. (2015) In vivo cell-cycle profiling in xenograft tumors by quantitative intravital microscopy. *Nat Methods* 12:577–585.

40. Shi J, Orth JD, Mitchison T (2008) Cell type variation in responses to antimitotic drugs that target microtubules and kinesin-5. *Cancer Res* 68:3269–3276.

41. Rowinsky EK, Donehower RC (1993) The clinical pharmacology of paclitaxel (Taxol). *Semin Oncol* 20(Suppl 3):16–25.

42. Thrower D, Jordan MA, Wilson L (1991) Quantitation of cellular tubulin in microtubules and tubulin pools by a competitive ELISA. *J Immunol Methods* 136:45–51.

43. Derry WB, Wilson L, Jordan MA (1995) Substoichiometric binding of taxol suppresses microtubule dynamics. *Biochemistry* 34:2203–2211.

44. Shannon KB, Canman JC, Ben Moree C, Tirnauer JS, Salmon ED (2005) Taxol-stabilized microtubules can position the cytokinetic furrow in mammalian cells. *Mol Biol Cell* 16:4423–4436.

45. Yang Z, Kenny AE, Brito DA, Rieder CL (2009) Cells satisfy the mitotic checkpoint in Taxol, and do so faster in concentrations that stabilize syntelic attachments. *J Cell Biol* 186:675–684.

46. Mitchison TJ (2012) The proliferation rate paradox in antimitotic chemotherapy. *Mol Biol Cell* 23:1–6.

47. Symmans WF, et al. (2000) Paclitaxel-induced apoptosis and mitotic arrest assessed by serial fine-needle aspiration: Implications for early prediction of breast cancer response to neoadjuvant treatment. *Clin Cancer Res* 6:4610–4617.

48. Mackenzie KJ, et al. (2017) cGAS surveillance of micronuclei links genome instability to innate immunity. *Nature* 548:461–465.

49. Harding SM, et al. (2017) Mitotic progression following DNA damage enables pattern recognition within micronuclei. *Nature* 548:466–470.

50. Mitchison TJ, Pineda J, Shi J, Florian S (2017) Is inflammatory micronucleation the key to a successful anti-mitotic cancer drug? *Open Biol* 7:170182.